

High Speed Mid-Wave Infrared Uni-traveling Carrier Photodetector

Jian Huang ^{1,2,3}, Zhiyang Xie ¹, Yaojiang Chen ¹, Baile Chen ^{1,*},

*Corresponding Author: Baile Chen (chenbl@shanghaitech.edu.cn)

¹ School of Information Science and Technology, ShanghaiTech University, Shanghai 201210, China

² Shanghai Institute of Microsystem and Information Technology, Chinese Academy of Sciences, Shanghai 200050, China

³ University of Chinese Academy of Sciences, Beijing 100049, China

Abstract: Mid-wave infrared (MWIR) frequency comb is expected to dramatically improve the precision and sensitivity of molecular spectroscopy. For high resolution application, high speed MWIR photodetector is one of the key components, however, the commercially available high speed MWIR photodetector only has sub-GHz bandwidth currently. In this paper, we demonstrate, for the first time to our knowledge, a high speed mid-wave infrared (MWIR) uni-traveling carrier photodetector based on InAs/GaSb type-II superlattice (T2SL) at room temperature. The device exhibits a cutoff wavelength of 5.6 μ m, and 3dB bandwidth of 6.58 GHz for a 20 μ m diameter device at 300K. These promising results show the device has potential to be utilized in high speed applications such as frequency comb spectroscopy, free space communication and others. The limitations on the high frequency performance of the photodetectors are also discussed.

Keyword: uni-traveling carrier photodetectors, high speed photodetectors, mid-wavelength infrared photodetectors, InAs/GaSb type II superlattices

Introduction:

Mid-infrared spectroscopy is a powerful tool to diagnose the composite of the chemicals due to the strong vibrational transition in the mid-infrared domain. Frequency combs in the mid-wave infrared domain bring a new set of tools for precision spectroscopy, which could be used to precisely investigate the changes of composition of a molecular sample over a large dynamic range¹⁻². High speed photodetector (PD) operated in MWIR range is one of the key components for the MWIR frequency comb application, which could significantly improve the resolution of the system. Besides that, high speed MWIR PDs are also demanded in the other emerging application areas such as free space communication ³⁻⁴ and mid-infrared light

detection and ranging (LIDAR) systems. Therefore, the development of high speed MWIR PD is essential in order to meet the increasing demands in these emerging areas. Technology based HgCdTe has made good progress in achieving high quantum efficiency and high sensitivity photodetectors. However, they are often operated at low temperatures and have a relatively low bandwidth, which is not suitable for high speed application⁵⁻⁶. Moreover, HgCdTe photodetectors are incompatible with the global initiative to eventually phase out the use of mercury. In recent years, high speed InSb photodetectors⁷, inter-band cascade infrared photodetectors (ICIPs)⁸⁻⁹, quantum cascade photodetectors (QCDs)¹⁰, and quantum well infrared photodetectors (QWIPs)¹¹⁻¹³ have been demonstrated. Ibrhim et al. reported an InSb p-i-n photodetectors grown on GaAs with an electrical 3dB bandwidth of 8.5GHz at room temperature⁷. Lotfi et al. showed a 1.3GHz 3dB bandwidth ICIP using InAs/GaSb/AlSb/InSb based type-II superlattices (T2SLs) as active layer and cutoff around 4.2μm at 300K⁸. Chen et al. demonstrated a 2.4GHz bandwidth ICIP employing an InAs/GaAsSb T2SLs absorption layer with a cutoff wavelength of 5.6μm at 300K⁹. The QCD structures have also achieved a 3dB bandwidth of 5GHz and with peak response wavelength of 4.5μm¹⁰. In addition, InGaAs/AlGaAs and GaAs/AlGaAs based QWIPs with RF response at 5GHz and peak wavelength of 4.9μm and 9μm respectively have also been demonstrated¹²⁻¹³.

In this work, we report the InAs/GaSb T2SL based uni-traveling carrier (UTC) photodiodes for MWIR high speed application. The UTC photodiode structure could overcome the slow transport of optical generated hole by using p-type absorber layer, where the optical generated holes can quickly be collected within the dielectric relaxation time, and only electron transit time dominates the total transit time of the device, thus it is expected to have higher speed than traditional PIN photodetector¹⁴⁻¹⁹. A 20μm-diameter device with 3dB bandwidth of 6.58 GHz and cutoff wavelength about 5.6μm at 300K is demonstrated. To the best of our knowledge, this is the first UTC photodetector demonstrated in MWIR band. The limiting factors of the 3dB bandwidth are also discussed by analyzing the small signal equivalent circuit of the devices.

Device Growth and Fabrication:

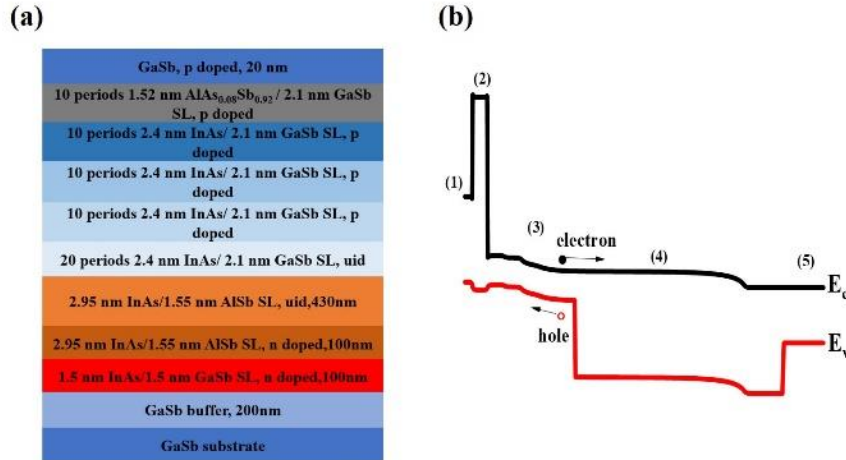


Figure. 1 (a) Epitaxial structure of the UTC PD. (b) Schematic band diagram of the UTC PD under zero bias. From left to right are: (1) top contact layer, (2) block layer, (3) graded absorption layer, (4) drift layer, (5) bottom contact layer. E_c and E_v represent conduction and valence band edge, respectively.

The epitaxial structure and band diagram of designed device are shown in Fig.1(a) and (b), respectively.

The sample was grown on a GaSb substrate by molecular beam epitaxy system (MBE), and the epitaxial growth started with a 200 nm thick GaSb buffer layer. After that, a 100nm n type ($1 \times 10^{18} \text{ cm}^{-3}$) InAs/GaSb superlattice (SL) bottom contact layer and 100nm n type ($1 \times 10^{18} \text{ cm}^{-3}$) InAs/AlSb SL layer were grown followed by a 430 nm thick un-intentionally doped (u.i.d.) InAs/AlSb SL drift layer. Then, a 50 periods InAs/GaSb SL grading p-doped absorption layer with doping concentration grading from $2 \times 10^{18} \text{ cm}^{-3}$ to uid was grown in order to have self-induced electric field to facilitate the electron transport. The followed is a 10 periods of p type ($2 \times 10^{18} \text{ cm}^{-3}$) AlAs_{0.08}Sb_{0.92}/GaSb SL as an electron blocking layer to prevent electrons in absorption layer diffusing to p type ($5 \times 10^{18} \text{ cm}^{-3}$) GaSb top contact layer.

Fig. 2(a) shows the high resolution X-ray diffraction (HRXRD) scan curves of the grown sample. A series of sharp satellite peaks were identified which indicated good crystal quality. The photoluminescence (PL) of the sample was measured at 77K as shown in Fig. 2(b). Here, a 532nm laser was used as excitation source and a step-scan Fourier transform infrared spectrometer (FTIR) equipped with MCT detector was used to detect the emission spectra. An emission peak around $4.4 \mu\text{m}$ was observed, which corresponding to the

transition between ground states in absorption layer. The PL spectra presented a narrow full-width at half-maximum (FWHM) of 16meV, which is also an indication of good crystalline quality.

After the material growth, the wafer was processed into a set of different sizes diameter mesa-shaped devices. Standard photolithography and citric-based wet chemical etchant were used to define mesa. Ti/Pt/Au (20 nm/20nm/80 nm) metal layers were deposited for both top and bottom contact layer to form ohmic contact by using e-beam evaporation, and mesa surfaces were passivated with SU-8. After that, a ground signal–ground (GSG) coplanar waveguide (CPW) pad with an air-bridge structure was electroplated on 2 μ m thickness SU-8 for high frequency measurement.

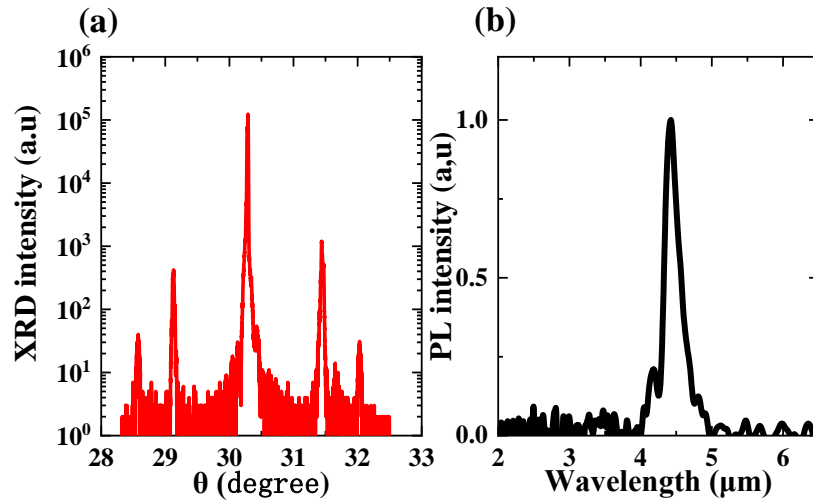


Figure 2. (a) High resolution XRD scan curve of the epi-structure. (b) Normalized PL spectra measurement of the sample at 77K.

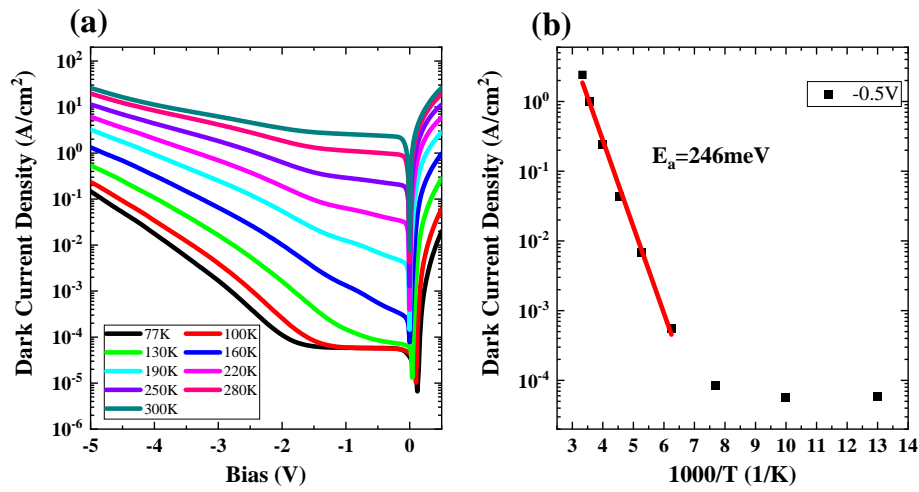


Figure 3. (a) Dark current density as a function of temperature of a 40 μ m diameter device. (b) Arrhenius plot of dark current density under -0.5V.

Measurement and analysis:

The temperature-dependent dark current density-bias voltage (J-V) characteristics of a 40 μm diameter device were measured and shown in Fig. 3(a). As temperature increases from 77K to 300K, dark current density varies from $5.77 \times 10^{-5} \text{ A/cm}^2$ to 2.4 A/cm^2 under -0.5V. Fig. 3(b) shows Arrhenius plot of temperature-dependent current density under -0.5V, the linear fit at high temperature region (160K-300K) yields an activation energy of 246 meV, which is close to the effective bandgap (about 275 meV to 221 meV from 77K to 300K) of InAs/GaSb SL absorption layer, indicating that dark current is dominated by diffusion component. At low temperature region (77K-130K), the dark current becomes temperature-insensitive, suggesting that dark current at low bias could be mainly contributed by surface leakage and background radiation in the low temperature station.

The responsivity spectra of the device were measured by a FTIR in top-illuminated configuration and calibrated by a blackbody source. Fig. 4(a) shows the responsivity of the device under zero bias from 77K to 300K, the fluctuations around 2.7 μm , 3.4 μm and 4.2 μm are due to water vapor and carbon dioxide gas absorption in the atmosphere. The cutoff wavelength of device at 77K is about 4.5 μm which is consistent to the peak wavelength of the PL result shown in Fig. 2(b) and the peak responsivity is about 0.5 A/W, as temperature increases to 300K the cutoff wavelength shifts to about 5.6 μm and the peak responsivity reduce to about 0.10 A/W. From 77K to 190K, the responsivity increases with temperature, this can be attributed to the shrink of InAs/GaSb SL effective bandgap, which causes a larger absorption. However, after temperature above 190K, the responsivity drops rapidly with increasing temperature, which results from the enhanced carrier recombination rate and lower carrier lifetime at high temperature. The specific detectivity D^* of the device was calculated by:

$$D^* = R_\lambda \sqrt{A} \left(2qI + \frac{4k_B T}{R} \right)^{-1/2} \quad (1)$$

where q is the electronic charge, k_B is Boltzmann's constant, T is the temperature of the device, R is the resistance under the bias, R_λ is the responsivity, I is dark current and A is the area of device. Fig. 4(b) shows D^* of the device under zero bias from 77K to 300K, a peak D^* of $2.5 \times 10^{11} \text{ cm} \cdot \text{Hz}^{1/2}/\text{W}$ was achieved at 77K. As temperature increases to 300K, the peak D^* decreases to about $3 \times 10^8 \text{ cm} \cdot \text{Hz}^{1/2}/\text{W}$.

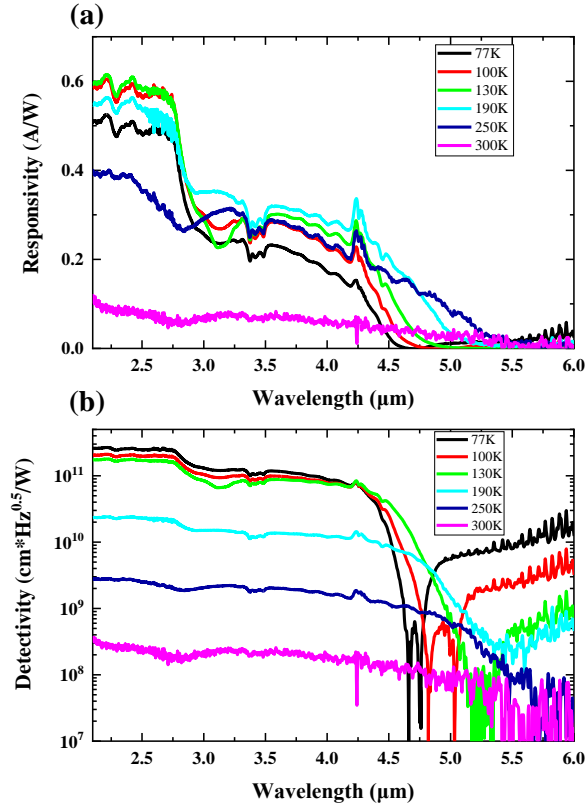


Figure. 4 (a)Responsivity and (b) specific detectivity of device under 0V from 77K to 300K.

For high speed characterization of the devices, a calibrated lightwave component analyzer (LCA) was used to test the bandwidth of the devices. Intensity-modulated light at 1550nm generated by LCA was focused by a lens fiber and coupled into the devices under test. The photoresponse of devices was collected by a Ground-Source-Ground (GSG) probe. The RF and DC components of the electrical signal were separated by RF bias tee, the RF signal was returned to LCA, and the DC part was connected to a source meter which provides DC bias and measures photocurrent.

Fig. 5(a) shows the frequency response of a 20μm diameter device under different bias at 300K. A bias-dependent response is observed, the 3dB bandwidth increase rapidly from 120MHz to 5.1GHz when bias changes from 0V to -2V as the InAs/AlSb drift layer is fully depleted. With bias further increases to -5V, the 3dB bandwidth reaches to 6.58GHz. The slight increasing 3 dB bandwidth with reverse bias beyond -2V is due to faster electron transport in the drift layer with increased reverse bias. By applying a higher reverse bias, the 3dB bandwidth could further increase, however, the increasing dark current will degrade the signal to ratio of the device and may also break down the device. Fig.5(b) shows the frequency response

of three devices with different sizes under -5V at 300K. The measured 3dB bandwidth of devices with diameter of 20 μ m, 40 μ m and 60 μ m are 6.58GHz, 5.62GHz and 3.39GHz, respectively. The weak diameter-dependent bandwidth indicates that the 3dB bandwidth of these devices should be dominated by transit time. To further investigate the bandwidth limit mechanism, we also measured S_{11} parameter of these devices. An equivalent circuit model shown in Fig. 6(a) was used to fit measured S_{11} parameter, where C_j is the junction capacitance, R_p is junction resistance, R_s is the series resistance, I_p is AC current source, R_L is load resistance. Fig. 6(b)-Fig. 6(d) shows the measured and fitting S_{11} curves of these three devices. With these extracted circuit model parameters, a theoretical RC time limited frequency response is plot in Fig.6 (e). The RC limited 3dB bandwidth of 20 μ m, 40 μ m and 60 μ m devices are calculated to be 27.85 GHz, 10.47GHz and 5.53 GHz, respectively. These RC limited bandwidth values are much larger than the corresponding measured bandwidth values for each size of devices, which indicates that the 3dB bandwidth of these devices is limited by carrier transit time. The extracted circuit model parameters are summarized in Table 1.

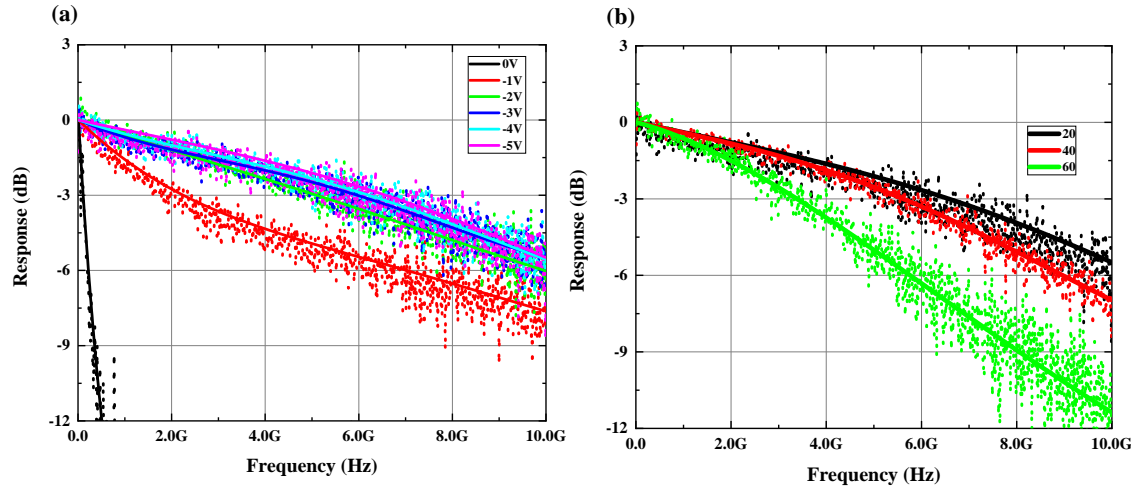


Figure.5 (a) Frequency response of a 20 μ m diameter device at various bias under 300K. (b) Frequency response of devices with different sizes under at -5V (dot line is the measured data and the solid line is polynomial fitting curve).

To further investigate transit process of the carries in device, the frequency response of a 20μm diameter device at different temperature and different bias was measured. Fig. 7(a) shows the measured frequency response under -5V from 77K to 300K, and the measured 3 dB bandwidth is summarized in Fig. 7 (b). As seen in Fig. 7(b), the 3 dB bandwidth verse temperature under different bias behaves differently. For device under low bias, such as -2V, 3 dB bandwidth increases significantly at high temperature. Under high reverse bias (such as -5V), 3dB bandwidth doesn't change significantly as temperature increases. That is mainly due to the unexpected conduction band discontinuity at the interface between absorption layer and drift layer. Under low bias condition, the unexpected barrier in conduction band could block the electrons transport. Thermal emission at higher temperature will help electrons to overcome the barrier. Under high bias condition, the barrier will not block the carrier transport, given the high electrical field in depletion region. The 3dB bandwidth is not sensitive to temperature in that case.

Table 1

Extracted parameters of device from equivalent circuit model

| Device diameter (μm) | C _j (fF) | R _p (Ohm) | R _s (Ohm) |
|---------------------------|---------------------|----------------------|----------------------|
| 20 | 70 | 6500 | 32.5 |
| 40 | 240 | 5000 | 14 |
| 60 | 500 | 3200 | 8.5 |

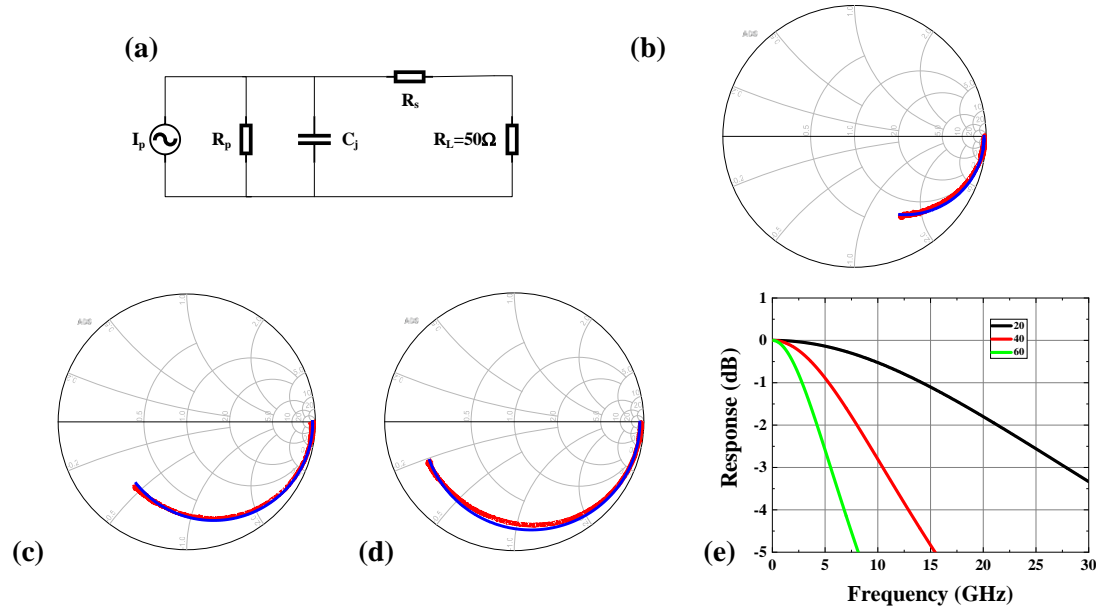


Figure. 6. (a) Equivalent circuit model of the UTC PD for S_{11} parameter fitting. Measured (red line) and fitting (blue line) S_{11} parameter from 10MHz to 30GHz of (b) 20μm, (c) 40μm and (d) 60μm diameter device under -5V. (e) Calculated RC limit frequency response with extracted circuit model parameters.

Based on the analysis above, the 3 dB bandwidth of the device is limited by electron transit time including the diffusion time in absorption layer and the drift time in drift layer. The unexpected conduction band discontinuity could also play a critical role to limit the device performance at the low bias and low temperatures. To further improve the speed of MWIR UTC PD, the InAs/AlSb drift layer should be further optimized to reduce the expected barrier between absorption layer and drift layer.

Table 2 summarized a performance comparison between high speed MWIR photodiodes with different structures or materials. It should note that some parameters in others works are not reported directly, and are extracted from the figures shown in the references. Comparing with others works, the 3 dB bandwidth of our device shows much higher performance. However, there are still remaining problems associated with the relatively small responsivity and slightly larger dark current for the UTC MWIR PDs as compared to interband cascade infrared photodetectors⁸. These issues could be potentially solved by using resonant cavity structure or waveguide structure²⁰. Moreover, the bandwidth can be further improved by engineering the design of the epitaxial layers, using highly resistive or semi-insulated substrate, reducing the device size, and applying waveguide structures to better balance between the bandwidth and the responsivity.

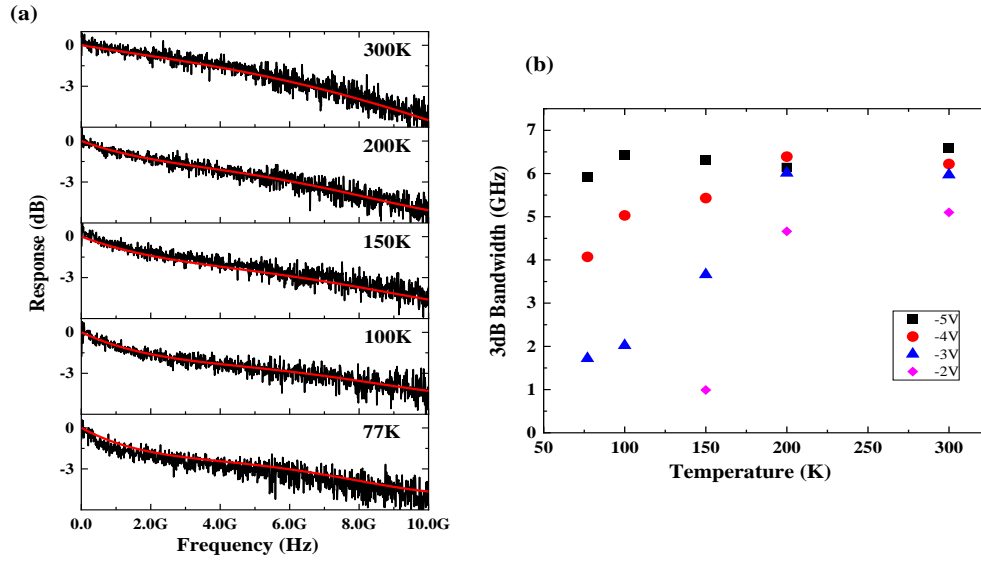


Figure. 7 (a) Measured frequency response of a 20μm diameter device under -5V at different temperature. (b) 3 dB bandwidth of a 20μm diameter device varies temperature under different bias.

Table 2
Performance comparison of high speed MWIR photodetectors, all data shown are at 300K or at room temperature

| Device parameters | Cutoff wavelength [μm] | DC density [A/cm ²] | Peak responsivity [A/W] | Peak D* [Jones] | 3dB bandwidth [GHz] |
|--------------------|------------------------|---------------------------------|-------------------------|---------------------------|---------------------|
| ICIP ₈ | 4.2 | 0.2(1 V) | 0.3 (0V) | 1.5×10 ⁹ (0V) | 1.3 |
| ICIP ₉ | 5.3 | 7 (-0.5 V) | 0.1 (0V) | NA | 2.4 |
| QWIP ₁₂ | 4.9 | NA | 0.1(-5V) | 1×10 ⁷ (-5V) | 5 |
| QWIP ₁₃ | 9 | 973.68 (-0.7V) | 0.08 (0.7V) | 3.3×10 ⁷ (0.7) | 5 |
| This work | 5.6 | 2.4 (-0.5V) | 0.1 (0V) | 3×10 ⁸ (0V) | 6.58 |

Conclusions:

In summary, an InAs/GaSb T2SL based MWIR UTC PD for high speed application has been demonstrated in this work. The cutoff wavelength of around 5.6μm and the 3dB bandwidth of 6.58 GHz are obtained for a 20μm diameter device at 300K. The equivalent circuit analysis shows the 3dB bandwidth of device is limited by transit time of optical generated carrier. With further material and device structure optimization, one can envision the prospects of using these UTC PDs in future free space optical communication, frequency comb spectroscopy and some other emerging areas requiring high speed MWIR receivers.

Acknowledgements

This work was supported by National Key Research and Development Program of China (2018YFB2201000, 2019YFB2203400); National Natural Science Foundation of China (61975121); Shanghai Sailing Program (17YF1429300) and ShanghaiTech University startup funding (F-0203-16-002).

References

- (1) Cruz, F. C.; Maser, D. L.; Johnson, T.; Ycas, G.; Klose, A.; Giorgetta, F. R.; Coddington, I.; Diddams, S. A. Mid-infrared optical frequency combs based on difference frequency generation for molecular spectroscopy. *Opt. Express* **2015**, *23*, 26814-26824.
- (2) Schliesser, A.; Picqué, N.; Hänsch, T. W. Mid-infrared frequency combs. *Nat. Photonics* **2012**, *6*, 440.
- (3) Manor, H.; Arnon, S. Performance of an optical wireless communication system as a function of wavelength. *Appl. Opt.* **2003**, *42*, 4285-4294.
- (4) Henniger, H.; Wilfert, O. An Introduction to Free-space Optical Communications. *Radioengineering* **2010**, *19*.
- (5) Rogalski, A. HgCdTe infrared detector material: history, status and outlook. *Rep. Prog. Phys.* **2005**, *68*, 2267.
- (6) Rogalski, A. Toward third generation HgCdTe infrared detectors. *Journal of alloys and compounds* **2004**, *371*, 53-57.
- (7) Kimukin, I.; Biyikli, N.; Kartaloglu, T.; Aytur, O.; Ozbay, E. High-speed InSb photodetectors on GaAs for mid-IR applications. *IEEE Journal of selected topics in quantum electronics* **2004**, *10*, 766-770.
- (8) Lotfi, H.; Li, L.; Lei, L.; Ye, H.; Shazzad Rassel, S.; Jiang, Y.; Yang, R. Q.; Mishima, T. D.; Santos, M. B.; Gupta, J. A. High-frequency operation of a mid-infrared interband cascade system at room temperature. *Appl. Phys. Lett.* **2016**, *108*, 201101.
- (9) Chen, Y.; Chai, X.; Xie, Z.; Deng, Z.; Zhang, N.; Zhou, Y.; Xu, Z.; Chen, J.; Chen, B. High-Speed Mid-Infrared Interband Cascade Photodetector Based on InAs/GaAsSb Type-II Superlattice. *J. Lightwave Technol.* **2019**.
- (10) Dougakiuchi, T.; Edamura, T. In *High-speed quantum cascade detector with frequency response of over 20 GHz*, SPIE Future Sensing Technologies, International Society for Optics and Photonics: 2019; p 111970R.
- (11) Palaferri, D.; Todorov, Y.; Bigioli, A.; Mottaghizadeh, A.; Gacemi, D.; Calabrese, A.; Vasanelli, A.; Li, L.; Davies, A. G.; Linfield, E. H. Room-temperature nine- μm -wavelength photodetectors and GHz-frequency heterodyne receivers. *Nature* **2018**, *556*, 85.
- (12) Rodriguez, E.; Mottaghizadeh, A.; Gacemi, D.; Palaferri, D.; Asghari, Z.; Jeannin, M.; Vasanelli, A.; Bigioli, A.; Todorov, Y.; Beck, M. Room-Temperature, Wide-Band, Quantum Well Infrared Photodetector for Microwave Optical Links at 4.9 μm Wavelength. *ACS Photonics* **2018**, *5*, 3689-3694.
- (13) Bigioli, A.; Gacemi, D.; Palaferri, D.; Todorov, Y.; Vasanelli, A.; Suffit, S.; Li, L.; Davies, A. G.; Linfield, E. H.; Kapsalidis, F. Mixing Properties of Room Temperature Patch-Antenna Receivers in a Mid-Infrared ($\lambda \approx 9 \mu\text{m}$) Heterodyne System. *Laser & Photonics Reviews* **2019**.
- (14) Nagatsuma, T.; Ito, H.; Ishibashi, T. High-power RF photodiodes and their applications. *Laser & Photonics Reviews* **2009**, *3*, 123-137.
- (15) Ito, H.; Kodama, S.; Muramoto, Y.; Furuta, T.; Nagatsuma, T.; Ishibashi, T. High-speed and high-output InP-InGaAs unitraveling-carrier photodiodes. *IEEE Journal of selected topics in quantum electronics* **2004**, *10*, 709-727.

- (16) Ito, H.; Furuta, T.; Kodama, S.; Ishibashi, T. InP/InGaAs uni-travelling-carrier photodiode with 310 GHz bandwidth. *Electron. Lett.* **2000**, *36*, 1809-1810.
- (17) Li, Z.; Pan, H.; Chen, H.; Beling, A.; Campbell, J. C. High-saturation-current modified uni-traveling-carrier photodiode with cliff layer. *IEEE Journal of Quantum Electronics* **2010**, *46*, 626-632.
- (18) Xie, Z.; Chen, Y.; Zhang, N.; Chen, B. InGaAsP/InP uni-travelling-carrier photodiode at 1064nm wavelength. *arXiv preprint arXiv:1906.06983* **2019**.
- (19) Ishibashi, T.; Furuta, T.; Fushimi, H.; Kodama, S.; Ito, H.; Nagatsuma, T.; Shimizu, N.; Miyamoto, Y. InP/InGaAs uni-traveling-carrier photodiodes. *IEICE transactions on electronics* **2000**, *83*, 938-949.
- (20) Craig, A.; Al-Saymari, F.; Jain, M.; Bainbridge, A.; Savich, G.; Golding, T.; Krier, A.; Wicks, G.; Marshall, A. Resonant cavity enhanced photodiodes on GaSb for the mid-wave infrared. *Appl. Phys. Lett.* **2019**, *114*, 151107.